

Convection patterns in a spherical fluid shell

F. Feudel and K. Bergemann

Institut für Physik und Astronomie, Universität Potsdam, Karl-Liebknecht-Strasse 24/25, D-14476 Potsdam-Golm, Germany

L. S. Tuckerman

PMMH (UMR 7636 CNRS - ESPCI - UPMC Paris 6 - UPD Paris 7), 10 rue Vauquelin, 75005 Paris, France

C. Egbers and B. Futterer

Department of Aerodynamics and Fluid Mechanics, BTU Cottbus, Siemens-Halske-Ring 14, D-03046 Cottbus, Germany

M. Gellert

Astrophysikalisches Institut Potsdam, An der Sternwarte 16, D-14467 Potsdam, Germany

R. Hollerbach

Department of Applied Mathematics, University of Leeds, Woodhouse Lane, Leeds, LS2 9JT, United Kingdom

(Received 13 July 2010; published 6 April 2011)

Symmetry-breaking bifurcations have been studied for convection in a nonrotating spherical shell whose outer radius is twice the inner radius, under the influence of an externally applied central force field with a radial dependence proportional to $1/r^5$. This work is motivated by the GeoFlow experiment, which is performed under microgravity condition at the International Space Station where this particular central force can be generated. In order to predict the observable patterns, simulations together with path-following techniques and stability computations have been applied. Branches of axisymmetric, octahedral, and seven-cell solutions have been traced. The bifurcations producing them have been identified and their stability ranges determined. At higher Rayleigh numbers, time-periodic states with a complex spatiotemporal symmetry are found, which we call breathing patterns.

DOI: [10.1103/PhysRevE.83.046304](https://doi.org/10.1103/PhysRevE.83.046304)

PACS number(s): 47.55.P-, 47.20.Bp, 47.20.Ky, 47.54.-r

I. INTRODUCTION

Motivated by the geophysical and astrophysical relevance of large-scale convection in planets and in outer zones of celestial bodies, the idealized model of spherical shell convection has long been the subject of intensive research in fluid dynamics. The motion of a fluid confined in a spherical shell under the influence of a central force and heated by a constant temperature from within is the classical Rayleigh-Bénard problem in spherical geometry. The question of pattern selection has been extensively studied by Busse and coworkers for both the nonrotating and rotating situations [1–4]. In particular, for nonrotating convection, the symmetry of the bifurcating branches and their stability are essentially determined by the degree ℓ of the spherical harmonics of the mode which becomes unstable.

The case we have investigated is motivated by the space experiment GeoFlow [5–8]. Our aim is to predict and analyze the convective patterns generated under microgravity conditions on the International Space Station (ISS). By means of the dielectrophoretic effect, a central force field with a $1/r^5$ radial dependence is generated and the experiment seeks to investigate thermal convection for both rotating and nonrotating spheres. The first theoretical investigations for this particular type of force field by exploitation of the dielectrophoretic mechanism for central field generation were performed by Yavorskaya *et al.* [9]. We will focus on the nonrotating case with special attention to symmetry-breaking pattern selection which is governed by the properties of the full spherical group.

Convection of a fluid in a spherical shell with radii $R_o > R_i$ heated from within and driven by buoyancy due to the central force field is governed by the Boussinesq equations in spherical geometry. By scaling length by R_o , time by the thermal diffusion time R_o^2/κ , where κ is the thermal diffusivity, and temperature by the imposed temperature difference between outer and inner sphere, the equations can be cast in nondimensional form:

$$\text{Pr}^{-1} \left[\frac{\partial \mathbf{u}}{\partial t} + (\mathbf{u} \cdot \nabla) \mathbf{u} \right] = -\nabla p + \nabla^2 \mathbf{u} + \frac{\text{Ra}T}{\beta^2 r^5} \mathbf{e}_r, \quad (1a)$$

$$\frac{\partial T}{\partial t} + \mathbf{u} \cdot \nabla T = \nabla^2 T, \quad (1b)$$

$$\nabla \cdot \mathbf{u} = 0, \quad (1c)$$

where \mathbf{e}_r is the radial unit vector and $\beta = (R_o - R_i)/R_i$ is the ratio of the thickness of the fluid shell to the inner radius. Corresponding to the GeoFlow experiment, the Prandtl number is set to $\text{Pr} = 64.64$, that of the silicone oil used. The aspect ratio β of the spherical shell is set to $\beta = 1.0$ so that the inner and outer surfaces are located at nondimensional radii $r_i = 1/2$ and $r_o = 1$. The boundary conditions imposed at the spherical surfaces are those corresponding to rigid and perfectly conducting spheres:

$$\mathbf{u} = 0 \text{ at } r = r_i, r_o; \quad (2a)$$

$$T = 1 \text{ at } r = r_i \quad \text{and} \quad T = 0 \text{ at } r = r_o. \quad (2b)$$

The objectives of this paper are to study the dynamics of the convection patterns, their bifurcations, and their stability as a

function of the Rayleigh number. For this purpose, a combined approach of simulations, linear stability computations, and bifurcation analysis has been applied. We use a spectral time-dependent code [10] to follow the evolution of the system from various initial conditions. In order to perform a bifurcation analysis, a path-following algorithm is incorporated which efficiently computes the stationary solutions via Newton's method [11,12].

In Sec. II we present several convection patterns which are obtained as time-asymptotic states by simulations. Starting from these states, essential parts of the bifurcation diagram were computed. A particular type of time-dependent solution with a complex spatiotemporal symmetry is examined in Sec. III. We finish in Sec. IV with a short summary and a discussion of some open questions.

II. STATIONARY CONVECTIVE PATTERNS

A. Background

For low Rayleigh numbers, the trivial heat conduction state is the only stable solution. The fluid is at rest and the spherically symmetric temperature profile is $T(r) = 1/r - 1$. The critical mode number characterizes the symmetry-breaking bifurcation by means of the equivariant branching lemma, which states necessary criteria for the existence of bifurcating branches with a given isotropy subgroup; an overview of this topic can be found in [13,14].

The implications for the spherical group by computing the dimensions of the fixed-point subspaces were first explored for $\text{SO}(3)$ by Michel [15] and extended to $\text{O}(3)$ by Ihrig and Golubitsky [16]. Further comprehensive reviews about spherically equivariant systems, their bifurcating branches, and their stability were published recently by Matthews [17,18]. In the case of $\text{O}(3)$ and ℓ even, all isotropy subgroups have an additional point inversion symmetry $\mathbf{r} \rightarrow -\mathbf{r}$, which commutes with all other group elements and is always present, and so will not be mentioned explicitly in the following.

The linear stability analysis carried out by Travnikov *et al.* [6,19] for aspect ratio $\beta = 1.0$ is summarized in Table I, which shows that the primary state becomes unstable at $\text{Ra} = 2491$ with critical mode number $\ell = 4$.

The equivariant branching lemma implies that for critical mode number $\ell = 4$, two branches, one axisymmetric with $\text{O}(2)$ symmetry and the other with octahedral symmetry, bifurcate transcritically. According to Chossat *et al.* [20] both branches must be unstable; however the octahedral branch is less unstable. Hence one expects that the octahedral branch, influenced by the nonlinear terms, would become generically stable near the primary bifurcation, via a turning point.

Another relevant investigation is that of Busse and Riahi [21]. These researchers predicted that when the thresholds of modes $\ell = 4$ and $\ell = 5$ were close, their interaction could yield

TABLE I. Critical Rayleigh numbers corresponding to the lowest spherical harmonic modes.

ℓ	1	2	3	4	5	6	7	8
Ra	9074	3897	2751	2491	2618	3018	3677	4618

a planform containing seven cells. The solution has fivefold rotational symmetry and an additional reflection symmetry about the meridional plane generating a D_5 symmetry. In addition there is a further reflection symmetry about the equatorial plane. Five cells are arranged around the equator and two at the north and south poles, leading to a total of seven cells.

B. Time-dependent simulations

The basis of our numerical tools is a spectral solver [10] which relies on the decomposition of the velocity field in toroidal and poloidal potentials:

$$\mathbf{u}(r,\theta,\phi,t) = \nabla \times f^{\text{Tor}} \mathbf{e}_r + \nabla \times \nabla \times f^{\text{Pol}} \mathbf{e}_r. \quad (3)$$

These potentials, as well as the temperature T , are further decomposed in terms of spherical harmonics Y_ℓ^m for the angular dependence and Chebyshev polynomials T_k for the radial dependence:

$$f(r,\theta,\phi,t) = \sum_{k\ell m} T_k \left[\frac{2r - (r_o + r_i)}{r_o - r_i} \right] P_\ell^m(\cos \theta) \times [f_{k\ell m}(t)e^{im\phi} + f_{k\ell m}^*(t)e^{-im\phi}]. \quad (4)$$

Spatial resolutions up to $(30, 40, 40)$ in (r, θ, ϕ) were used, and time steps of $\Delta t = 10^{-4}$. The time-stepping algorithm uses a modified Crank-Nicolson formula for the diffusive terms and a second-order Runge-Kutta scheme for the remaining terms.

We will use several target functions to demonstrate some of the dynamical features. The total kinetic energy of the fluid E_{kin} , the energies $E(\ell)$ associated with modes of degree ℓ ,

$$E_{\text{kin}} = \frac{1}{2} \int |\mathbf{u}|^2 dV = \sum_{\ell} E(\ell), \quad (5)$$

and the Nusselt number Nu ,

$$\text{Nu} = \frac{1}{4\pi} \int_{r=1} \frac{\partial T}{\partial r} dS, \quad (6)$$

are global quantities. The particular coefficient

$$|A|^2 \equiv |f_{k=0,\ell=2,m=2}^{\text{Tor}}|^2 \quad (7)$$

of the expansion (3)–(4) is used to distinguish between fields which differ only by their angular orientation, and so have the same E_{kin} , $E(\ell)$, and Nu . [Note that while the decomposition of a field into different degrees ℓ is well defined, the further decomposition into different orders m depends on the choice of axis. It is for this reason that (7) is useful in distinguishing fields with different orientations.]

The nonlinear computations confirm that the conductive state loses stability for a Rayleigh number $\text{Ra} > 2491$ where the $\ell = 4$ mode becomes excited. In Fig. 1 the onset of convection is demonstrated by a simulation ramping the Rayleigh number above its critical value to $\text{Ra} = 2500$ starting from the conductive regime. The contour plots present snapshots of the radial velocity component, which is closely related to the temperature field in the middle of the spherical gap. This simulation agrees with the mathematical results discussed in Sec. II A in that both axisymmetric and octahedral components play a role in this transition, and that only the octahedral state is asymptotically stable at $\text{Ra} = 2500$. The

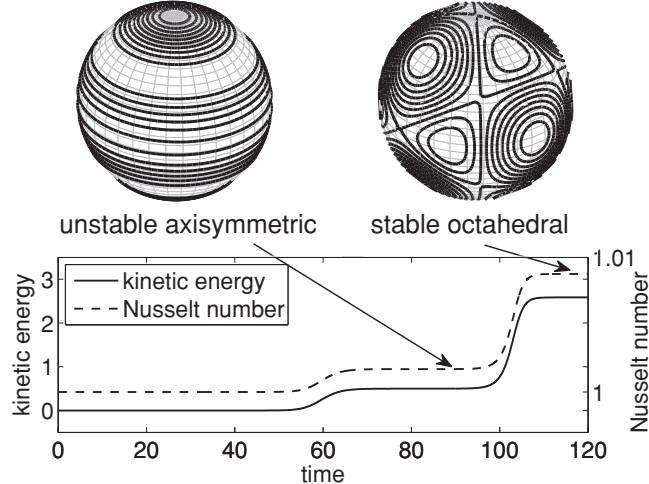


FIG. 1. Snapshots of the transient after ramping the Rayleigh number to $\text{Ra} = 2500$ from the conductive state. The contour plots depict the radial velocity component in the middle of the spherical gap at time $t_1 = 80$ (left top) and $t_2 = 120$ (right top). The corresponding time-dependence of the kinetic energy and of the Nusselt number, respectively, are presented at the bottom.

long-lasting axisymmetric phase indicates both the dominance of axisymmetric perturbations in the initial condition and also the existence of a weakly unstable axisymmetric solution; this will be confirmed in Sec. II C. The time dependence of the Nusselt number depicted in Fig. 1 demonstrates the enhancement of the heat transfer in the last phase when the octahedral mode becomes dominant.

Searching for other stationary solutions, we have performed further simulations with different initial conditions and at various Rayleigh numbers. We have located another stable solution branch with fivefold rotational symmetry, shown in Fig. 2, which we take to be the seven-cell pattern mentioned

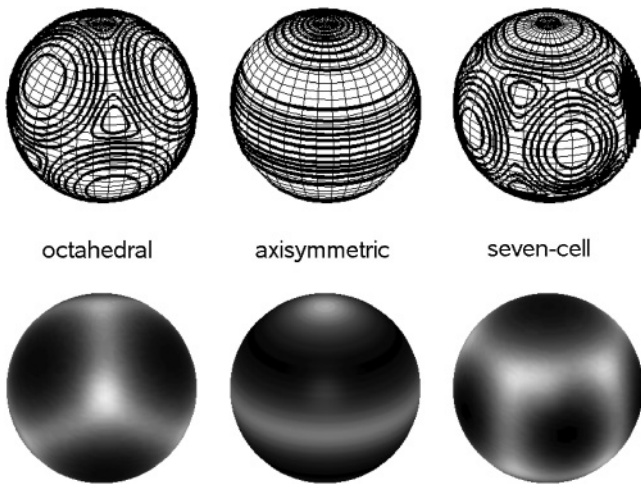


FIG. 2. Time-asymptotic stationary states at $\text{Ra} = 9000$. Both upper and lower rows depict the radial velocity at mid-gap, with dark levels corresponding to down-welling motion. Upper row: simple contour plot. Lower row: shadow contour plot. From left to right: octahedral, axisymmetric, and fivefold symmetric (seven-cell) patterns.

in Sec. II A predicted by Busse and Riahi [21] resulting from the interaction between $\ell = 4$ and $\ell = 5$ modes. Indeed, a decomposition into spherical harmonics of our solution shows that the most important kinetic energy contributions are from $\ell = 4$ followed by $\ell = 5$. For $\text{Ra} = 9000$, the $\ell = 5$ contribution to the kinetic energy is about half that of $\ell = 4$.

Summarizing the simulations, three stable solutions have been found. These are presented in Fig. 2 at $\text{Ra} = 9000$ where all three patterns are stable simultaneously. The octahedral group leaves both the octahedron and the cube invariant with respect to its symmetry operations. Identifying the dark patches of the lower left plot in Fig. 2 with surfaces of a cube, one recognizes this feature. The seven-cell structure of the fivefold rotational pattern in the right column of Fig. 2 can also be identified. As mentioned in Sec. II A, the axisymmetric state in the middle of Fig. 2 is unstable near onset; indeed, Fig. 1 shows the axisymmetric solution appears only as a transient, demonstrating its unstable nature at $\text{Ra} = 2500$. Since it is found as a time-asymptotic pattern at $\text{Ra} = 9000$, a stabilizing bifurcation must occur at some intermediate Rayleigh number.

In order to clarify the generation and stabilization of different solution branches, a more systematic bifurcation analysis will be presented in the next subsection.

C. Bifurcations and stability of stationary solution branches

In order to better understand the bifurcations, a path-following method was applied by means of which the stationary branches can be traced systematically. To do so, the time-stepping code is modified as described in [11,12] and summarized briefly below. We write Eqs. (1a)–(1c) schematically as

$$\frac{\partial \mathcal{U}}{\partial t} = (\mathcal{L} + \mathcal{N})\mathcal{U}, \quad (8)$$

where $\mathcal{U} \equiv (\mathbf{u}, T)$. The time-stepping code is first modified to carry out first-order Euler time stepping, implicit for the diffusive operators and explicit for the remaining terms, which we write as

$$\mathcal{U}(t + \Delta t) = \mathcal{U}(t) + \Delta t(\mathcal{L}\mathcal{U}(t + \Delta t) + \mathcal{N}\mathcal{U}(t)). \quad (9)$$

Equation (9) is rearranged to read

$$\begin{aligned} \mathcal{U}(t + \Delta t) - \mathcal{U}(t) &= (I - \Delta t\mathcal{L})^{-1}(I + \Delta t\mathcal{N})\mathcal{U}(t) - \mathcal{U}(t) \\ &= (I - \Delta t\mathcal{L})^{-1}\Delta t(\mathcal{L} + \mathcal{N})\mathcal{U}(t). \end{aligned} \quad (10)$$

The roots of the operator on the right-hand-side of (10) are found by using Newton's method, each step of which calculates a decrement $\delta\mathcal{U}$ to the current estimate \mathcal{U} by solving

$$\begin{aligned} (I - \Delta t\mathcal{L})^{-1}\Delta t(\mathcal{L} + D\mathcal{N}_{\mathcal{U}})\delta\mathcal{U} \\ = (I - \Delta t\mathcal{L})^{-1}\Delta t(\mathcal{L} + \mathcal{N})\mathcal{U}, \end{aligned} \quad (11)$$

$$\mathcal{U} \leftarrow \mathcal{U} - \delta\mathcal{U}.$$

The linear system (11) involves the Jacobian $D\mathcal{N}_{\mathcal{U}}$ of \mathcal{N} evaluated at \mathcal{U} and is solved by the biconjugate gradient method [22], which converges rapidly without requiring the formation or storage of the Jacobian matrix.

The time-asymptotic states obtained in simulations were used as initial estimates for Newton's method and the resulting branches were computed for both decreasing and increasing

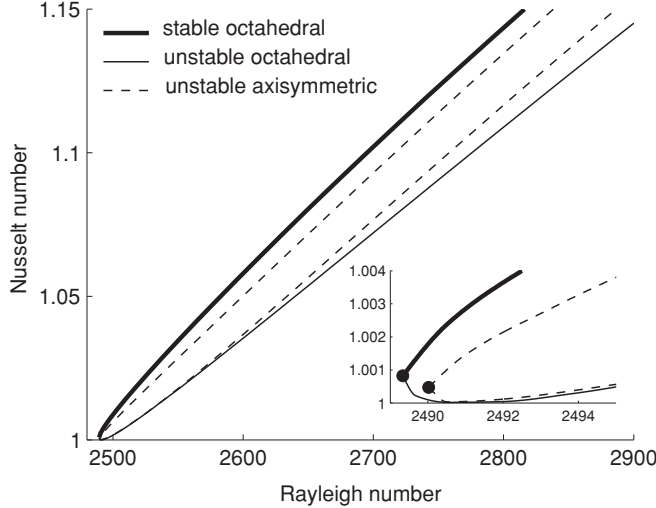


FIG. 3. Transcritical symmetry-breaking bifurcation at the critical Rayleigh number.

Rayleigh numbers. We are able to trace branches around turning points and a complex net of stationary branches can be constructed in this way. It is usually not possible to construct a complete bifurcation diagram containing all bifurcations and branches and so we restrict our search to the branches connected to the patterns found in the time-dependent simulations. For a more detailed description of how this procedure can be effectively implemented in the Navier-Stokes solver we refer to [23,24]. The stability ranges were determined by calculating the growth or decay rates of perturbations about the steady states and interpolating to determine the Rayleigh numbers at which these rates cross zero.

We begin by showing the onset of convection in Fig. 3, which depicts the Nusselt number vs the Rayleigh number. Four branches are visible for $\text{Ra} > \text{Ra}_{\text{cr}}$ in Fig. 3, one stable and three unstable branches. As predicted by the mathematical results cited in Sec. II A, the bifurcation is transcritical, has critical mode $l = 4$, and leads to both octahedral and axisymmetric branches. Both branches have turning points slightly below the critical Rayleigh number. In accordance with the predictions by Chossat *et al.* [20] the octahedral branch becomes stable while the axisymmetric branch remains unstable in these saddle node bifurcations.

Figure 4 is a continuation of Fig. 3. Since the Nusselt number depends linearly on Ra and differs only weakly between the different branches presented in Fig. 4, we plot instead the function $(\text{Nu} - 1)/\text{Ra}$ in order to better differentiate the branches. In addition, we represent the bifurcation diagram schematically in Fig. 5. The stable octahedral branch and both axisymmetric branches are shown, but the unstable octahedral branch is not involved in this portion of our study and so is omitted from these figures. The stable octahedral branch undergoes no bifurcations and remains stable over the entire Ra interval presented, until $\text{Ra} = 23\,400$.

One of the two initially unstable axisymmetric branches, that with the smaller Nusselt number, becomes stable at $\text{Ra} = 4493$ and remains so until $\text{Ra} = 18\,665$. The flows along this branch contain four toroidal rolls, with upwelling fluid at

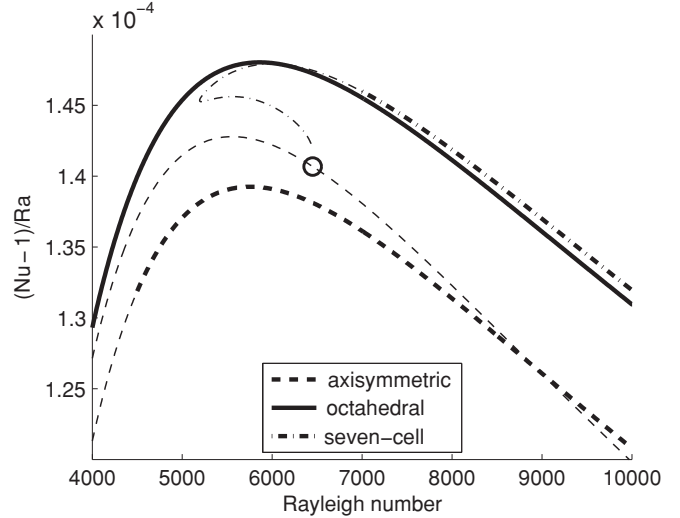


FIG. 4. The stable octahedral branch, both axisymmetric branches, and the bifurcating fivefold symmetric (seven-cell) branch are represented by the rescaled Nusselt number. Thick lines mark stable solutions while thin lines designate unstable branches. The open circle marks the subcritical pitchfork bifurcation leading to the seven-cell state.

the poles and equator, and downwelling at midlatitudes. The other axisymmetric branch remains unstable and the states belonging to it have downwelling motion at the poles and equator. It is from this branch that the fivefold symmetric (seven-cell) state found in our simulations and seen in Fig. 2 originates, bifurcating subcritically at $\text{Ra} = 6450$. This branch undergoes a turning point at $\text{Ra} = 5194$ and eventually becomes stable at $\text{Ra} = 7150$, remaining so until $\text{Ra} = 17\,450$. Its Nusselt number increases along the branch, eventually

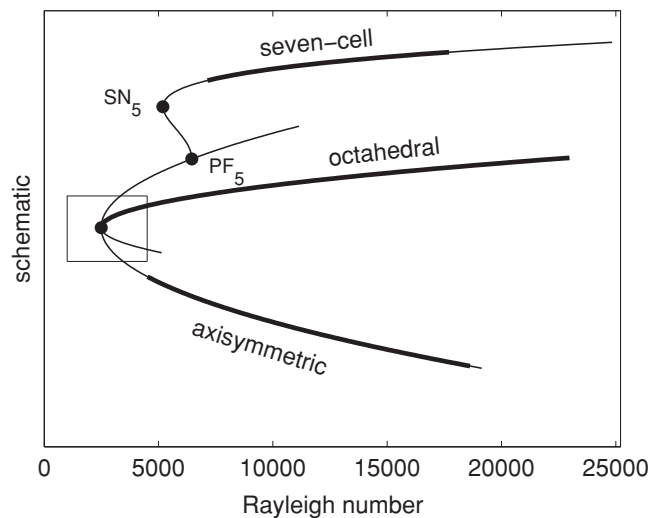


FIG. 5. Schematic bifurcation diagram illustrating the stabilization of one of the axisymmetric branches and the creation and stabilization of the fivefold symmetric (seven-cell) branch. Thick and thin curves indicate stable and unstable branches, respectively, and dots indicate bifurcations. The square surrounds the primary bifurcation generating the octahedral and axisymmetric branches depicted in Fig. 3, whose transcritical nature is too weak to be resolved on this scale.

exceeding that of all the branches in Fig. 4. Except for the subcritical bifurcation creating the fivefold symmetric branch, the crossings of different branches in Fig. 4 are only projection effects and do not correspond to genuine intersections.

In summary, as a result of this scenario, of the branches presented in Fig. 2, three remain stable over a fairly large interval of Ra: the octahedral branch ($2489.7 < \text{Ra} < 23\,400$), the axisymmetric branch ($4493 < \text{Ra} < 18\,665$), and the fivefold symmetric seven-cell branch ($7150 < \text{Ra} < 17\,450$). We note that in simulations of the Swift-Hohenberg equation on a spherical surface with critical mode numbers $\ell = 6, 8$, or 10 , Matthews [18] finds considerable ranges of multistability, involving axisymmetric states and states with D_ℓ or icosahedral symmetry. In conclusion, it is likely that multistability, including stabilization of the axisymmetric branch, is a generic feature of symmetry breaking of the full spherical O(3) group, such as occurs in convection in a spherical layer in a central force field.

The flows which are not stationary are the topic of the next section.

III. TIME-DEPENDENT CONVECTION PATTERNS

Increasing the Rayleigh number further, the dynamics eventually become time dependent. In order to describe this regime in more detail we will examine a representative simulation at $\text{Ra} = 23\,500$.

Initializing the simulation at $\text{Ra} = 23\,500$ with random conditions leads to a time-asymptotic state, time series from which are shown in Fig. 6. The kinetic energy of the fluid, shown in the top row, and the Nusselt number of the heat flux through the outer sphere, shown in the middle row, vary periodically in time. Moreover the energy of each mode ℓ has the same frequency, corresponding to a period of $\tau = 1.075$ in dimensionless units, as shown in Fig. 7. This energy is a sum over the poloidal and toroidal components and, beyond this, the sum over all $m \in [-\ell, \ell]$. The bottom of Fig. 6 shows that the coefficient defined in (7) has a periodicity which is five

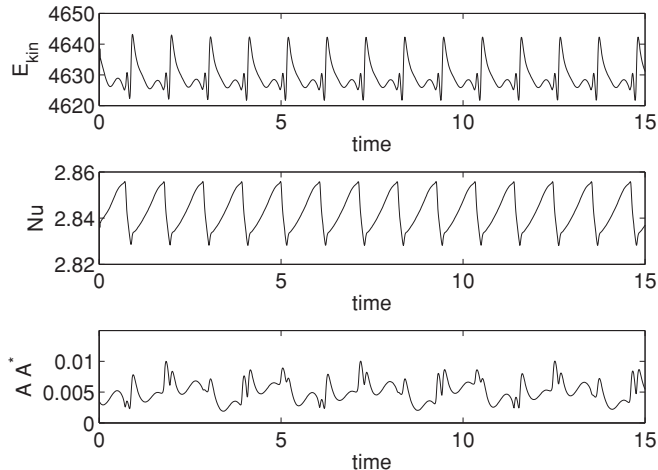


FIG. 6. The kinetic energy (top), the Nusselt number of the heat flux through the outer sphere (middle), and the absolute square of a particular mode amplitude $|A|^2 \equiv |f_{022}^{\text{Tor}}|^2$ (bottom) as a function of time at $\text{Ra} = 23\,500$.

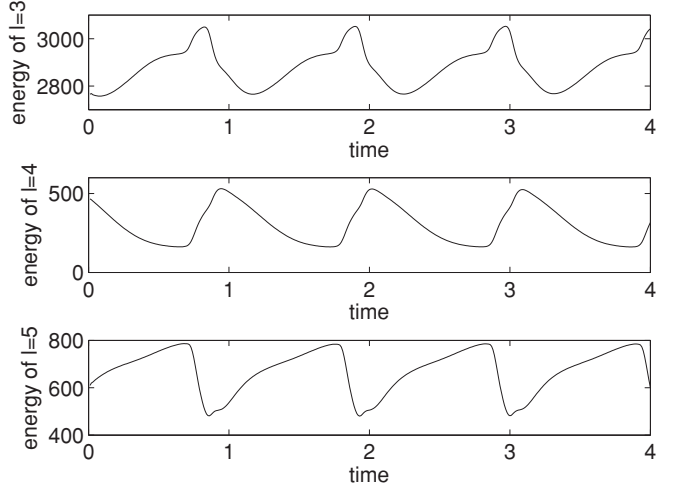


FIG. 7. Energy in modes $\ell = 3, 4$, and 5 as a function of time at $\text{Ra} = 23\,500$.

times that of the kinetic energy, the Nusselt number, and each ℓ mode. This would imply a spatiotemporal symmetry of the flow, perhaps as a result of a Hopf bifurcation under certain symmetry constraints.

Figure 8 presents contour plots of the radial velocity over the smaller period, $\tau = 1.075$. The first snapshot is taken at the moment of maximum kinetic energy, at $t_0 = 4.13$; see Fig. 6. In order to trace the evolution of the pattern in time, these snapshots are taken at nonuniform time intervals. Since the kinetic energy varies rapidly at the end of its period, cf. Fig. 6, a feature which is accompanied by more drastic changes of the convection pattern, the three snapshots in the lower row of Fig. 8 are chosen from this time range. Reconstructions of the contour lines give an impression of the evolution of the pattern. The last snapshot presents the pattern at time τ after the initial snapshot, but it differs from the initial snapshot. This corroborates the last row of Fig. 6: The pattern, like the individual spectral coefficients, varies over a period longer than τ . However, by applying a rotation of the sphere, we have verified that the convection pattern at time $t = t_0$ is a rotated



FIG. 8. Contour plots of the radial velocity for $\text{Ra} = 23\,500$ at time points $t_0 = 4.13$, $t_1 = t_0 + 0.4\tau$, $t_2 = t_0 + 0.8\tau$, $t_3 = t_0 + 0.9\tau$, $t_4 = t_0 + 0.95\tau$, and $t_5 = t_0 + \tau$ from left to right and from top to bottom.

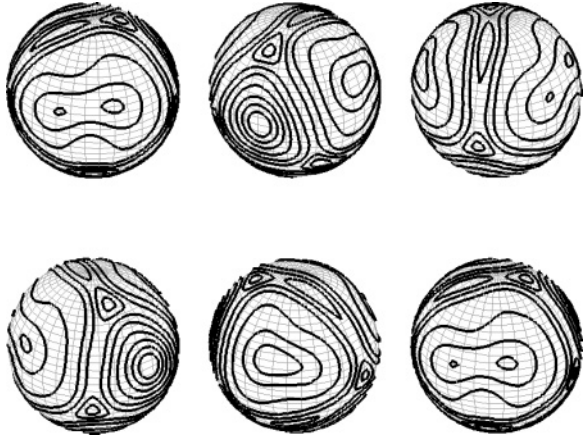


FIG. 9. Contour plots of the radial velocity for $\text{Ra} = 23\,500$ over the entire spatiotemporal cycle: $t_0 = 4.13$, $t_1 = t_0 + \tau$, $t_2 = t_0 + 2\tau$, $t_3 = t_0 + 3\tau$, $t_4 = t_0 + 4\tau$, and $t_5 = t_0 + 5\tau$ from left to right and from top to bottom.

version of that at $t = t_0 + \tau$. For instance, the triangle-shaped side surface in the last snapshot can be recovered in the first snapshot on the back side of the sphere.

The dynamics of the entire spatiotemporal cycle are illustrated in Fig. 9, which extends Fig. 8 by showing six snapshots differing by intervals of τ . After 5τ , the original convection pattern appears again at the same position on the sphere, completing the spatiotemporal cycle.

Since the convection pattern does not move like a wave along the sphere but rather changes its shape in time more like a breather, we call these particular solutions breathing patterns (BP). An interesting feature of these solutions is a remnant of a tetrahedral structure in the convection pattern which, while not perfect, can be seen in the last snapshot in Fig. 8 and in the second, third, and fourth ones in Fig. 9. A mode analysis yields a strong dominance of the $\ell = 3$ mode in the spectrum followed by the $\ell = 5$ and $\ell = 4$ mode. These exchange energy periodically in time as presented in Fig. 7. All the other modes oscillate with a much smaller amplitude. The $\ell = 3$ mode dominance is certainly correlated with the tetrahedral-like structure, cf. Refs. [3,21].

In order to better understand the transition from the stationary to the time-dependent solutions we traced this BP branch downward diminishing the Rayleigh number stepwise. In order to reveal qualitative changes in the limit cycles we plot the kinetic energy of mode $\ell = 5$ versus that of $\ell = 3$ in Fig. 10 for six selected Rayleigh numbers. Starting with a Rayleigh number of $\text{Ra} = 23\,500$ the first subfigure presents the solution of the BP branch for which the spatiotemporal symmetry is described above. The closed orbit corresponds to the smaller period (Figs. 7 and 8) which the trajectory circles five times before completing the entire spatiotemporal cycle (bottom panel of Figs. 6 and 9). The BP branch remains stable, periodic in time, and does not change qualitatively until Ra is lowered past 21 000. For lower Rayleigh numbers the original orbit loses stability and the trajectories look chaotic, as depicted for $\text{Ra} = 20\,900$ and $\text{Ra} = 19\,500$ in Figs. 10 and 11,

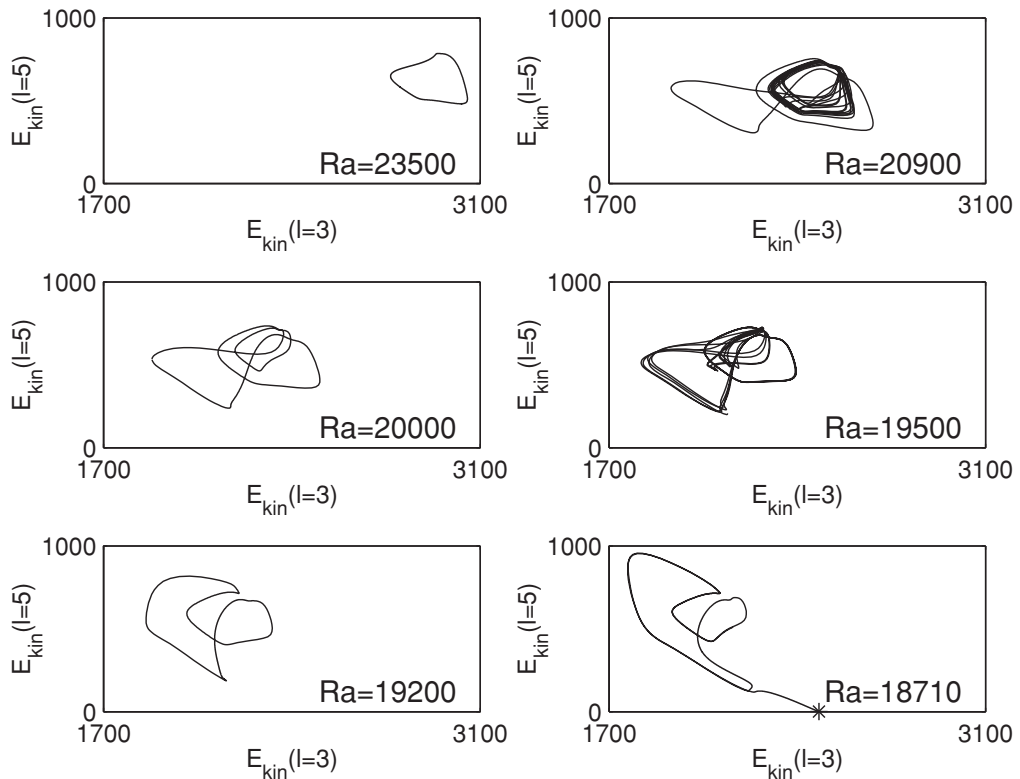


FIG. 10. The kinetic energies of mode $\ell = 5$ vs. $\ell = 3$ for diminishing Rayleigh numbers from left to right and from top to bottom. The star in the last panel ($\text{Ra} = 18\,710$) marks the asymptotic position of the frozen states. The orbit structure reflects the nature and position of the attractor.

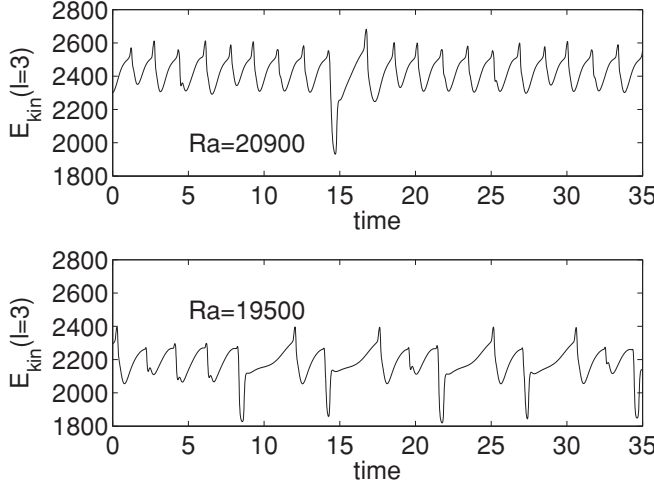


FIG. 11. Time series for chaotic regimes at $\text{Ra} = 20\,900$ and at $\text{Ra} = 19\,500$. In the time series for $\text{Ra} = 20\,900$, one recognizes the nearly periodic dynamics with occasional excursions.

showing larger excursions away from the original region of the BP branch. This chaotic region is interrupted by short windows in which more complex periodic attractors can be found, e.g., at $\text{Ra} = 20\,000$. The chaotic feature of the time-dependent solutions disappears for $\text{Ra} < 19\,400$ and a qualitatively new periodic branch becomes stable for smaller Rayleigh numbers. The shape of the closed orbit, an example of which is depicted for $\text{Ra} = 19\,200$ in Fig. 10, resembles the structure of the original chaotic attractors. The smallest Rayleigh number for which we could find a periodic attractor was for $\text{Ra} = 18\,720$.

Figure 12 shows the Rayleigh number dependence of the periods of the limit cycles depicted in Fig. 10 via the frequency $1/\tau$. The period shown is that of the E_{kin} or $E(\ell)$ variation; we do not take into account rotation of the pattern. Two features of Fig. 12 are evident. First, the limit cycles that we have computed belong to several different branches. The abrupt variation of the frequency between $\text{Ra} = 20\,400$ and $\text{Ra} = 21\,000$ and between $19\,400$ and $20\,000$ coincides with the

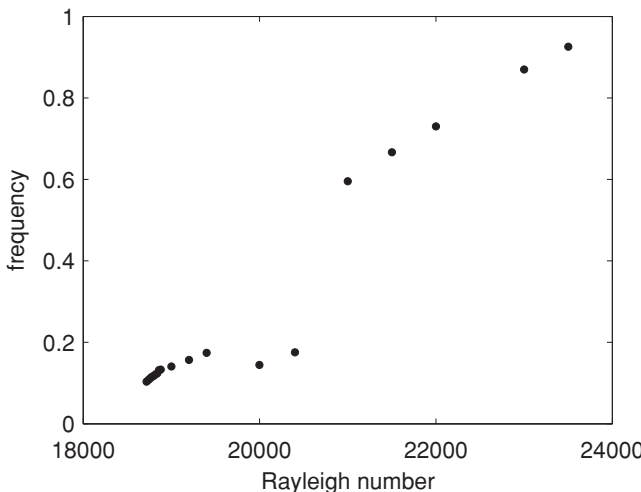


FIG. 12. Frequency of kinetic energy oscillation as shown in Fig. 7 as a function of Rayleigh number.

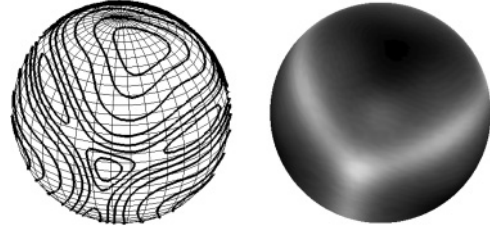


FIG. 13. Convection pattern of the branch of frozen states (four-cell pattern) at $\text{Ra} = 18\,600$. Left: contour plot. Right: corresponding shadow contour plot, with bright levels marking upwelling motion.

changing nature of the limit cycles seen in the phase portraits of Fig. 10. Second, the frequency seems to approach zero (the period seems to diverge) as Ra decreases. This would indicate a disappearance via some type of global bifurcation.

The last subfigure in Fig. 10 supports this idea, since it demonstrates for $\text{Ra} = 18\,710$ how the trajectory escapes from the periodic attractor and settles down to a nearly stationary solution, whose position is depicted by a star. We denoted these solutions frozen states. The trajectory seems to approach a fixed point solution, converging, however, very slowly. The last figures of the global functions are still changing systematically after a simulation of hundreds of thermal diffusion times. Figure 13 presents the final convection state after the pattern no longer changes. The tetrahedral symmetry is obviously discernible. A mode analysis gives a strong dominance of the $l = 3$ mode combined with an additional excitation of the $l = 4$ mode. This mixed-mode pattern caused by this mode interaction was also predicted by Busse and Riahi [21] as an additional stable solution in spherical geometry which they called a four-cell pattern. It possesses a tetrahedral symmetry, similar to the pure $l = 3$ pattern (cf. Ref. [3]). We were able to reach these frozen states by diminishing the Rayleigh number starting from time-dependent solutions. Moreover, these states could not be used as initial estimates for Newton iteration. This is probably because the very slow convergence implies that states reached via time-dependent simulation are insufficiently close to the underlying steady states.

Going upward in Ra , we have found that periodic or chaotic solutions that are qualitatively similar to those in the interval $18\,720 \leq \text{Ra} \leq 23\,500$ persist until at least $\text{Ra} = 30\,000$. However, a quantitatively accurate study of these solutions would require increased spatial resolution.

In summary, the transition from the stationary states to time-dependent solutions and its reverse route is very complex. It is certainly also essentially governed by the spherical symmetry. We were able to describe several of the time-dependent features, such as the appearance of the spatiotemporal symmetry. However, the transitions undergone by the time-dependent states bring up in turn new questions which can only be answered by more extensive future investigations.

IV. DISCUSSION

In this work, symmetry-breaking convection in a central forced spherical fluid shell is described. By applying the equivariant branching lemma for a spherically symmetric geometry, the nature of the primary bifurcation leading to the onset of the convection can be classified. Our numerical computations

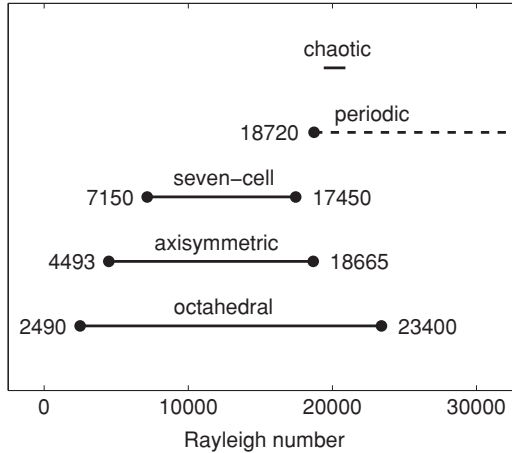


FIG. 14. Stability ranges of steady and time-dependent states. The upper limit of the periodic states has not been determined, nor the intervals over which time-dependent states are chaotic.

confirm this transcritical bifurcation. The bifurcating branches, an octahedral branch and an axisymmetric branch, both have turning points slightly below the critical Rayleigh number. The octahedral branch becomes stable at this turning point whereas the axisymmetric branch remains unstable. Nevertheless, for slightly supercritical Rayleigh numbers, one can observe extremely long axisymmetric transients.

With respect to GeoFlow, in which a central force field with a $1/r^5$ dependence was realized experimentally, the first results showed the octahedral pattern which appears in the supercritical region over a wide Rayleigh number range.

Further simulations starting with different initial conditions at higher Rayleigh numbers produce several time-asymptotic stationary solutions with different symmetries: octahedral, axisymmetric, and fivefold symmetric, all coexisting and

stable over a large Rayleigh-number range. In order to explain this multistability, a more systematic bifurcation analysis by means of path-following tools has been performed. Essential parts of the bifurcation diagram were computed and the origin of the stable stationary solution branches appear as the result of further symmetry-breaking bifurcations.

For higher Rayleigh numbers, our simulations led to an interesting time-dependent attractor, which we called a breathing pattern (BP). The BP states possess a complex spatiotemporal symmetry which is probably also dictated by the spherical group. In an intermediate Rayleigh-number range, time-dependent states—periodic and chaotic—coexist with steady patterns. As a guide, Fig. 14 summarizes the stability ranges of the various steady and time-dependent states we have found and demonstrates the multistability present in this system. The derivation of amplitude equations describing the origin of the time-dependent states is left for future investigation.

In conclusion, we believe that much of the scenario that we have described is generic for convection problems in nonrotating spherical shells. For the usual $1/r^2$ gravitational force, we would not expect to find the same critical Rayleigh number values, but we would expect qualitative agreement. We hope that these detailed investigations can help to identify the underlying mechanisms which drive the transitions from laminar to spatiotemporal patterns in spherical geometry.

ACKNOWLEDGMENTS

The support of this work by the ESA in the framework of the GeoFlow project is gratefully acknowledged. We thank Paul Matthews for his insightful comments about the manuscript. F. Feudel thanks Philippe Beltrame for fruitful discussions about symmetry breaking in equivariant branching theory.

-
- [1] F. H. Busse, *J. Fluid Mech.* **72**, 67 (1975).
[2] N. Riahi, G. Geiger, and F. H. Busse, *Geophys. Astrophys. Fluid Dyn.* **20**, 307 (1982).
[3] F. H. Busse and N. Riahi, *J. Fluid Mech.* **123**, 283 (1982).
[4] M. Ardes, F. H. Busse, and J. Wicht, *Phys. Earth Planet. Inter.* **99**, 55 (1997).
[5] C. Egbers, W. Beyer, A. Bonhage, R. Hollerbach, and P. Beltrame, *Adv. Space Res.* **32**, 171 (2003).
[6] V. Travnikov, C. Egbers, and R. Hollerbach, *Adv. Space Res.* **32**, 181 (2003).
[7] P. Beltrame, V. Travnikov, M. Gellert, and C. Egbers, *Nonlin. Processes Geophys.* **13**, 413 (2006).
[8] B. Futterer, C. Egbers, S. Koch, N. Dahley, and L. Jehring, *Acta Astronaut.* **66**, 193 (2010).
[9] I. M. Yavorskaya, N. I. Fomina, and Y. N. Belyaev, *Acta Astronaut.* **1**, 179 (1984).
[10] R. Hollerbach, *Int. J. Num. Methods Fluids* **32**, 773 (2000).
[11] C. K. Mamun and L. S. Tuckerman, *Phys. Fluids* **7**, 80 (1995).
[12] L. S. Tuckerman and D. Barkley, in *Numerical Methods for Bifurcation Problems and Large-Scale Dynamical Systems*, edited by E. Doedel and L. S. Tuckerman (Springer, New York, 2000).
[13] M. Golubitsky, I. Stewart, and D. G. Schaeffer, *Singularities and Groups in Bifurcation Theory*, Vol. II (Springer, New York, 1988).
[14] P. Chossat and R. Lauterbach, *Methods in Equivariant Bifurcations and Dynamical Systems* (World Scientific, Singapore, 2000).
[15] L. Michel, *Rev. Mod. Phys.* **52**, 617 (1980).
[16] E. Ihrig and M. Golubitsky, *Physica D* **13**, 1 (1984).
[17] P. C. Matthews, *Nonlinearity* **16**, 1449 (2003).
[18] P. C. Matthews, *Phys. Rev. E* **67**, 036206 (2003).
[19] V. Travnikov, Ph.D. thesis, BTU Cottbus, 2004.
[20] P. Chossat, R. Lauterbach, and I. Melbourne, *Arch. Ration. Mech. Anal.* **113**, 313 (1990).
[21] F. H. Busse and N. Riahi, *Nonlinearity* **1**, 379 (1988).
[22] H. van der Vorst, *SIAM J. Sci. Stat. Comput.* **13**, 631 (1992).
[23] K. Borońska and L. S. Tuckerman, *Phys. Rev. E* **81**, 036320 (2010).
[24] K. Borońska and L. S. Tuckerman, *Phys. Rev. E* **81**, 036321 (2010).